Editors' Suggestion | Featured in Physics

Active-Hydraulic Flows Solve the Six-Vertex Model (and Vice Versa)

Camille Jorge* and Denis Bartolo†
Univ. Lyon, ENS de Lyon, Univ. Claude Bernard, CNRS, Laboratoire de Physique, F-69342, Lyon, France

(Received 15 October 2024; accepted 10 March 2025; published 7 May 2025)

By confining colloidal active fluids in microchannel networks, we demonstrate that their degenerate flows correspond to the configurations of the six-vertex model. We use this quantitative correspondence to control and explain the active flows that emerge in square-grid networks. In particular, we show that the Lagrangian trajectories of active particles realize the Baxter-Kelland-Wu mapping and form completely packed loops, whose geometry can be exactly predicted and explained. We then go beyond the square-grid geometry and introduce a general framework for predicting the geometry of active-hydraulic flows in arbitrary networks.

DOI: 10.1103/PhysRevLett.134.188302

From the 2D Ising model to quantum spin chain, exactly solvable models are rarely intended to provide accurate descriptions of real-life experiments. One of their essential values is to reveal profound connections between seemingly unrelated areas of physics and mathematics. The six-vertex model offers a compelling example [1,2]. This model was inspired by Pauling's early work, and intended to gain some insight into the residual entropy of water ice [3]. It consists in assigning different statistical weight to the six vertices drawn in Fig. 1(a), and to place them on the square lattice. Although it cannot explain actual ice-calorimetry measurements, the six-vertex model has become a cornerstone of mathematical physics. It has indeed revealed strong links between fields as diverse as Coulomb gas physics, percolation theory, ferroelectricity, polymer physics, loop models, quantum hall physics, conformal field theory, and combinatoric and stochastic processes; see, e.g., [4–9].

Here, we show that the six-vertex model provides an accurate description of active matter experiments. Confining colloidal active fluids in hydraulic networks, we establish experimentally a quantitative correspondence between the active flow field and the spin configurations of the six-vertex model. We then use this one-to-one correspondence to quantitatively explain the seemingly random geometry of active hydraulic flows in square-grid networks. We show that the Lagrangian trajectories associated with the flows form Baxter-Kelland-Wu loops, and quantitatively explain their self-similar morphologies [10]. Informed by our findings, we conclude with the presentation of a comprehensive set of active-hydraulic laws that should predict the geometry of active flows in arbitrarily complex networks.

*Contact author: camille.jorge@ens-lyon.fr
†Contact author: denis.bartolo@ens-lyon.fr

In our experiments, we use 2D active fluids assembled from Quincke rollers of diameter 5 μm [11]. As illustrated in Fig. 1(b), we first confine them in a square-grid network made of 1800 straight channels (width 200 μm); see [12] for a detailed presentation of the experimental methods and Supplemental Material (SM) for experiments performed in different geometries [13]. As we turn on the electric motors that power the self-propulsion of our Quincke rollers, they self-assemble into an active liquid whose spontaneous flows quickly reach a steady state illustrated in Figs. 1(b) and 1(c) and Supplemental Videos 1 and 2.

The steady flows are homogeneous. We find that the number density is narrowly peaked on $\rho_0 = 8,500\ \mathrm{mm}^{-2}$, and that the particle flux J hardly fluctuates around two possible values $J = \pm J_0$, where $J_0 = 1300\ \mathrm{s}^{-1}$; see Figs. 1(d) and 1(e) and [24]. The resulting flow patterns can therefore be accurately described by using the sign of J to orient the edges of the graph formed by the channel network; see Fig. 1(e) and [25]. However, repeating the same experiment, with the same colloids, in the same geometry, yields different patterns, all having a seemingly random geometry. In this Letter, our goal is to explain the morphology of these emergent flows. To achieve this goal, we identify an essential active-hydraulic rule that has been hitherto overlooked, and show how to systematically map active flows on exactly solvable statistical mechanics models.

We can indeed make an important progress by noting that the geometry of the current field at the nodes exactly corresponds to the six vertices of the six-vertex model [Fig. 1(a)]. This observation is a direct consequence of the two constraints imposed on all confined active flows. They were first identified by Woodhouse and Dunkel in [25], and confirmed in a number of experiments: (i) when confined in sufficiently slender channels the flows of active fluids are laminar and operate at constant speed set by the level of activity of the materials [24,26–28]; (ii) mass is conserved.

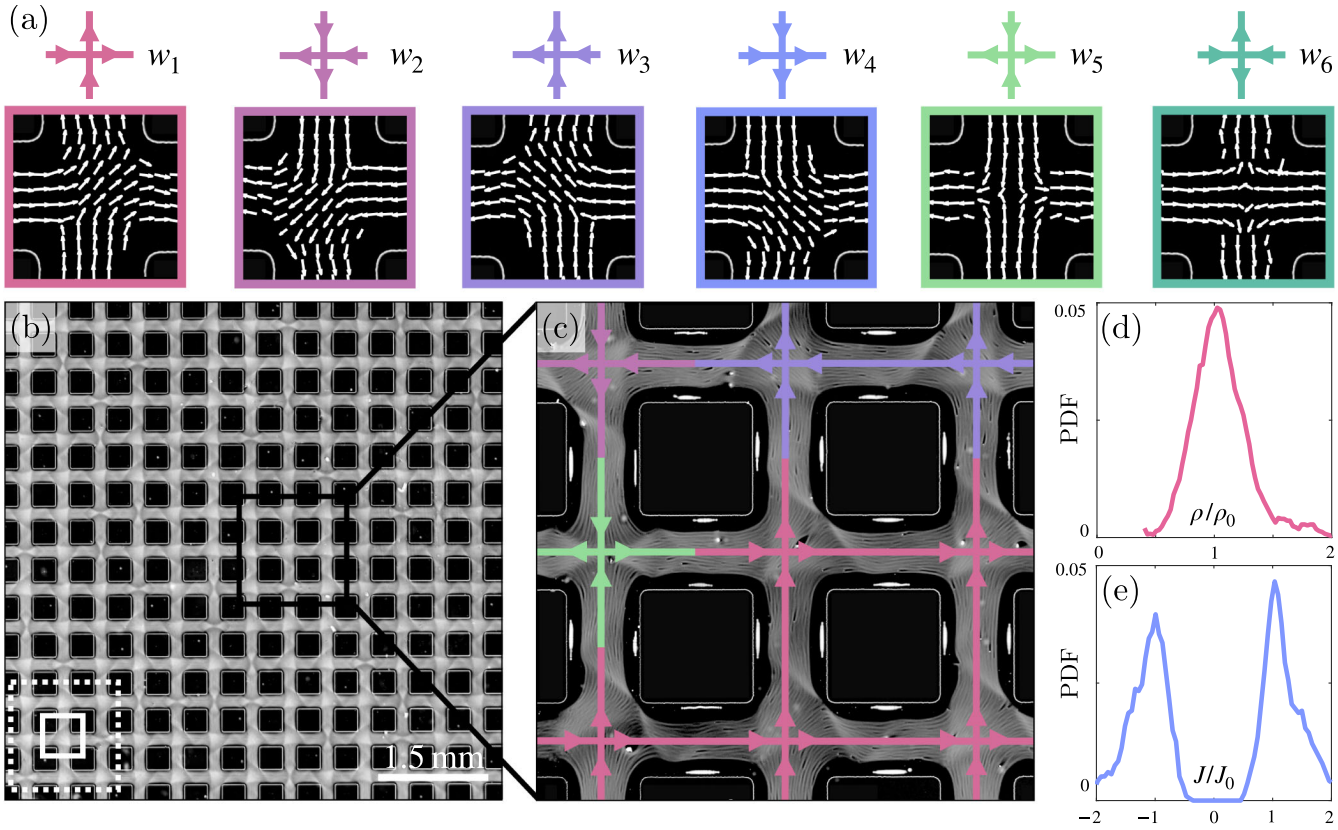

FIG. 1. The six-vertex-model rules are realized by active hydraulics flows. (a) Top row: illustrations of the vertices of the six-vertex models. The w_i are their statistical weights. Bottom row: velocity field at the nodes of the channel network. The six possible flow configurations are in a one-to-one correspondence with the six-vertex model. (b) Active fluid assembled from colloidal rollers confined in a square grid of identical channels. The white squares illustrate the relative sizes of the whole grid (dashed line) and of the picture of the 13×13 channels (solid line). The active flow is stationary. (c) A superimposition of subsequent images shows the trajectories of the active colloids. The arrows indicate the direction of the flow, and the colors indicate the type of vertices; see (a). (d) Probability density function (PDF) of the colloid density, ρ measured in all the channels of the network. The number density is normalized by its average values $\rho_0 = 8500\ \mathrm{mm}^{-2}$. (e) PDF of the current, J. The current value is normalized by its average value $J_0 = 1300 \pm 260\ \mathrm{s}^{-1}$.

Therefore, in steady state, when the density heterogeneities have relaxed, activity and mass conservation impose

$$J_{\langle i,j\rangle} = \pm J_0, \tag{1}$$

$$\sum_j J_{\langle i,j\rangle} = 0 \tag{2}$$

at every edge $\langle i, j\rangle$ and node i. In other words, in all networks with a fourfold coordination, irrespective of the channel and node geometry, all vertices must obey the two-in-two-out rule illustrated in Fig. 1(a). Equations (1) and (2) are, however, not sufficient to explain our active-hydraulic flows. These equations define the vertices of a vertex model [2,29] but not their statistical weight. Whereas early theories assumed that they had equal probabilities [12,25,30,31], our measurements do not confirm this spin-ice hypothesis. After repeating the same experiment 10 times, we count the occurrences of each vertex and measure their statistical weight w_i, $i = 1, \ldots, 6$. We find that they are not identical: $w_1 = w_2 = w_3 = w_4 = 0.20 \pm 0.01$, while $w_5 = w_6 = 0.09 \pm 0.01$. These weights are not only material-dependent but also strongly depend on the geometry of the junctions between the straight channels; see also SM [13]. To see this, we add cylindrical posts at each junction [Fig. 2(a)] and measure the evolution of the w_is with the post radius r [Fig. 2(b)]. For all radii, we have $w_1 = w_2 = w_3 = w_4$ and $w_5 = w_6$ as expected from the axisymmetry of the post shape. But Fig. 2(b) shows that $w_5 + w_6$ monotonically increases from $\simeq 0.18 \pm 0.03$ to 1 as r increases. From a fluid mechanics perspective, this result is intuitive: adding a solid obstacle at a junction favors the formation of a stagnation point. The variations of the w_i's are, however, not anecdotal. They are accompanied by a qualitative evolution of the macroscopic flow patterns as shown in Figs. 2(d), (e) and SM [13]. To explain the geometries of the spontaneous flows, we make a second key observation. Equations (1), (2) and the $\{w_i\}$ fully specify the statistics of the flow field: our active-hydraulic experiment generates independent configurations of the

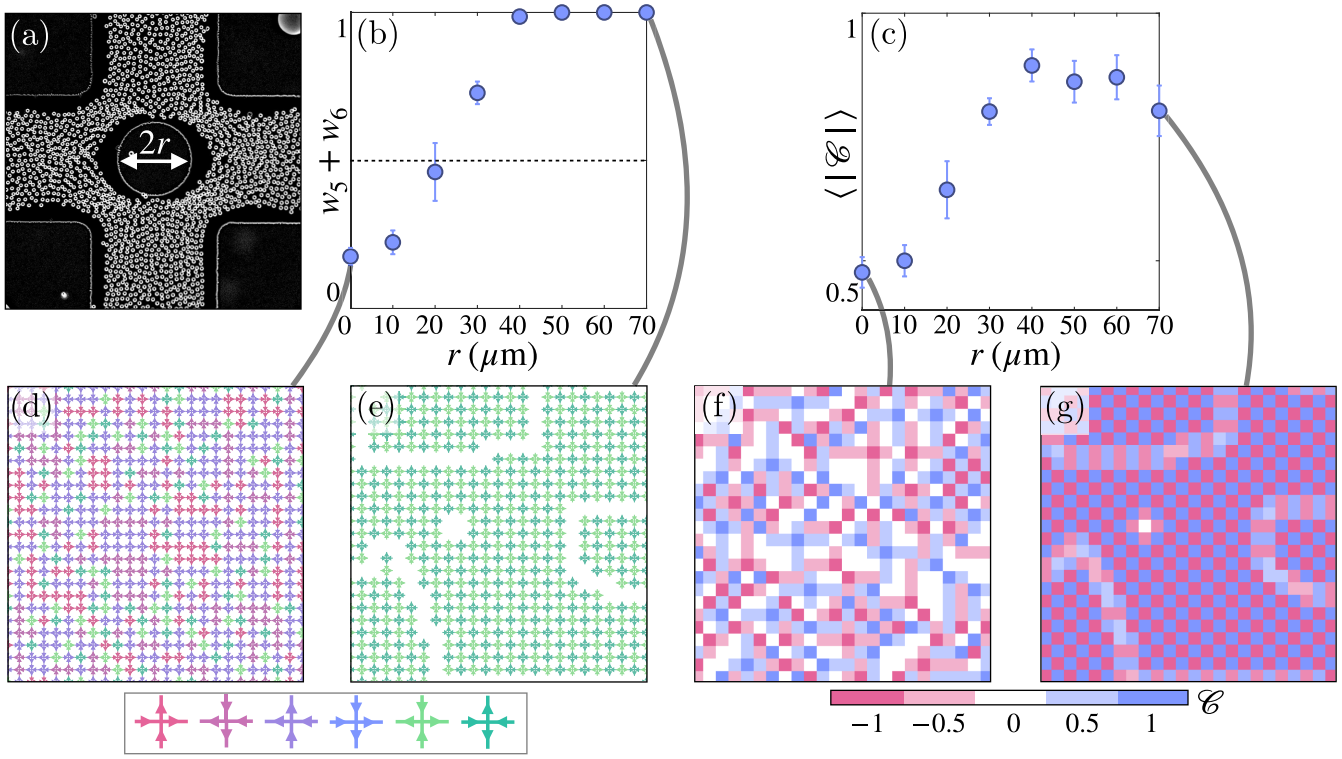

FIG. 2. Weight of the six vertices and order-to-disorder transition. (a) Image of a junction with a circular post of radius $r = 70$ μm. (b) Evolution of $w_5 + w_6$ with the post radius r. The dashed line corresponds to $w_5 + w_6 = \frac{1}{2}$. (c) Evolution of the average circulation $\mathcal{C} = \langle|\mathcal{C}_p|\rangle_p$, where C_p is the circulation around the p th plaquette. (d) Example of a flow field measured in an experiment where $r = 0$ μm. (e) Example of a flow field measured in an experiment where $r = 70$ μm. When r is large, the flow only includes vertices of type 5 and 6. (f) Circulation field measured in an experiment where $r = 0$ μm (disordered). (g) Circulation field measured in an experiment where $r = 70$ μm (ferroelectric phase).

six-vertex model. We can therefore use the large body of knowledge on this integrable model to quantitatively explain the morphology of our hydraulic patterns. A first well-established result concerns the phase behavior of the six-vertex model. When $(w_5 + w_6) = \frac{1}{2}$ theory predicts an order-to-disorder transition between an antiferroelectric and an isotropic phase. We do observe this structural transition. Antiferroelectric order corresponds to edge fluxes of alternate signs, or equivalently to plaquettes of alternate circulations [32,33]. In Fig. 2(c) we plot the evolution of the average circulation $\mathcal{C}$ as a function of the post radius r. We show the circulation field for $r = 0$ μm and $r = 70$ μm in Figs. 2(f) and 2(g). We find a clear sign of a transition when $w_{5,6}(r) = \frac{1}{2}w_{1-4}(r)$ [Fig. 2(b)]. This phase transition has clear consequences on the geometry of the hydraulic flows and, in particular, on their Lagrangian trajectories illustrated in Fig. 3(a).

In the ordered state, the active fluid circulates around the plaquettes and only two stationary flows can exist (away from possible domain walls). The resulting Lagrangian trajectories obviously reduce to closed loops of length 4; see Supplemental Video 3. The disordered phase is mode subtle: it corresponds to a critical phase where seemingly random fluctuations correlate over system-spanning scales. To better understand its geometry, we track the active colloids and plot their trajectories at the two type of vertices in Fig. 3(b). We find that the Quincke rollers propel along trajectories that realize the so-called Baxter-Kelland-Wu mapping from the six-vertex to the completely packed loop model; see [10] and SM [13] for a basic introduction to this mapping. This observation readily tells us that the Lagrangian trajectories should form soups of closely packed self-avoiding loops, in good agreement with our observations [Fig. 3(a)]. Predicting the geometry of the emergent flows therefore amounts to determining the statistics of the loop geometry. We explain in SM [13] how to quantitatively describe these geometries thanks to a series of mappings between the six-vertex, completely packed loop, and bond percolation models [10]. These (exact) theories predict that the largest loop has the same statistics as the hull of the percolation cluster at criticality [34]. It has a self-similar shape and its gyration radius (defined by $R_g^2 = \langle \mathbf{r_e} - \langle \mathbf{r_e} \rangle \rangle^2$, where $\mathbf{r_e}$ is the position of the e th edge in a given loop), scales as $R_g \sim L^\nu$ with $\nu = 4/7$ [Fig. 3(c)]. All the other loops are less crumpled and their gyration radius is that of self-avoiding polymers with $\nu = 3/4$ [34–36]. We also find that the probability of finding a Lagrangian trajectory of

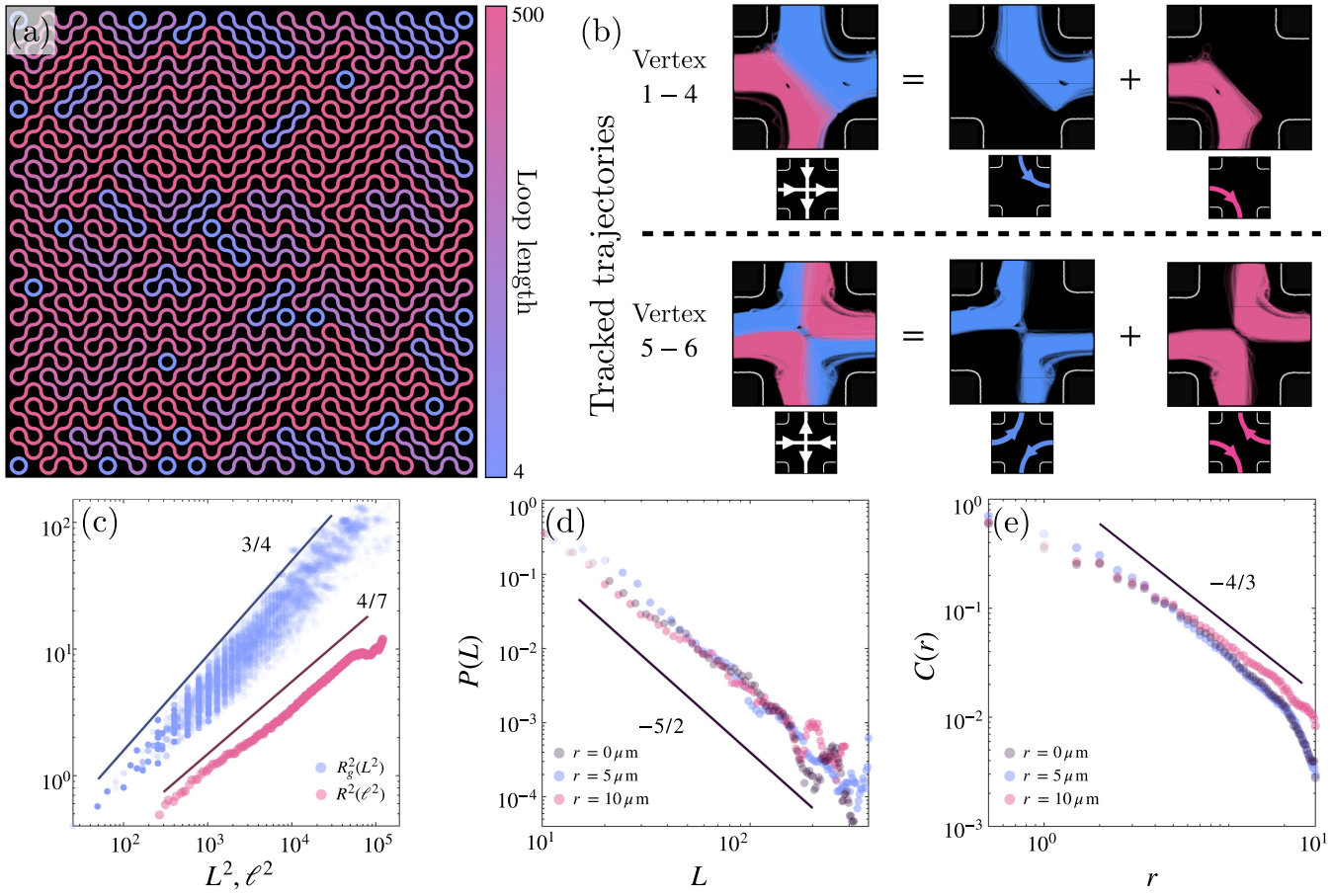

FIG. 3. Lagragian trajectories, self-avoiding loops, and geometry of the disordered flows. (a) Experimental Lagrangian trajectories of the active flow in the disordered regime (no circular post). The trajectories are constructed from the experimental flow field using the rules obeyed by the rollers at every node; see (b). The colors indicate the lengths of the loops. (b) Tracked trajectories of the colloidal rollers. Labeling the trajectories with two colors, we find a direct correspondence with the Baxter-Kelland-Wu mapping from the six-vertex-model configurations to closely packed loops on the square lattice [10]. 93% of the 155 000 trajectories we have tracked follow these rules. (c) Symbols: gyration radius R_g of the Lagrangian trajectories plotted versus their length L. Blue symbols: all loops but the largest. Solid lines: theoretical predictions of the ν exponent. Pink symbols: largest loop measured in each experiments. For better statistics for the largest loop, we plot the mean square distance $R^2(\ell^2) = \langle|\mathbf{r}(s) - \mathbf{r}(s+\ell)|^2\rangle_s$, where $\mathbf{r}(s)$ is the position measured at the curvilinear coordinate s along the loop. $R^2(L^2)$ and $R_g^2(\ell^2)$ obey the same scaling laws. (d) Probability $P(L)$ of finding a loop of length L in the ensemble formed by the Lagrangian trajectories. Symbols: experiments. Solid line: theoretical prediction. (e) Two point correlation function $C(r)$. It is defined as the probability of finding two points separated by a distance r within the same loop. Symbols: experiments. Solid line: theoretical predictions. (d), (e) The three colors correspond to three different post radii ($r = 0, 5, 10$ μm). The statistics corresponds to ten independent realizations of the experiment. The collapse of our data indicate that all the disordered flows belong to the same universality class.

length L should scale as $P(L) \sim L^{-5/2}$ [34,37] [Fig. 3(d)]. Lastly, the two point correlation function $C(r)$ that corresponds to the probability of finding two points at a distance r within the same loop should scale as $C(r) \sim r^{-4/3}$ [34,37] [Fig. 3(e)]. Figure 3(c) compares these analytical predictions to our experimental measurements. The agreement is excellent. We therefore conclude that the vertex rules of Fig. 1(a) define the laws of active hydraulics in tetravalent pipe networks. From a dual perspective, our experiments show that the Quincke rollers collectively solve the six-vertex model.

We close our Letter with a more general discussion. Solving hydrodynamic equations or particle-based models would limit the predictive power of simulations to networks composed of a handful of channels. We propose to solve this computational problem by introducing a comprehensive set of active hydraulics rules, beyond the specifics of the square-grid network. We construct these rules from the results presented above and in Ref. [12]. They apply to networks made of channels of identical cross sections but having arbitrarily complex geometries. (i) The first rule is given by mass conservation, Eq. (1). (ii) The second rule is the active-flow law and generalizes Eq. (1). In general, the

local current can take three different values $J_{\langle i,j\rangle} = -J_0, 0, +J_0$ [25]. When $J = 0$, the active fluid flows at the subchannel scale but forms vortices and do not support any net flux [12]. (i) implies that at least one of the edge currents vanishes at every node having an odd coordination number: laminar flows are geometrically frustrated [12,30]. We note that this frustration can also have a dynamical origin as seen in Fig. 2(g) where the domain walls between incompatible antiferroelectric regions host localized vortices. (To predict the morphology and statistics of the domain walls, the vertex rules of Fig. 1(a) should be complemented by 13 additional vertices, including an even number of edges where $J = 0$. This corresponds to the 19-vertex model that has also been extensively studied; see, e.g., [38].) Rules (i) and (ii) define vertex rules. However, as in all vertex problems, they must be complemented by the statistical weights of the vertices (iii) and interactions rules (iv). (iii) Statistical weights of the vertices: they must be measured experimentally as in Fig. 2 and SM [13]. These weights are not determined by first principles and are not material properties either. They are determined by the microscopic geometry of the nodes. A simple control strategy consists of adding flow splitters to bias the flow statistics, and promote spatial order as exemplified in Figs. 2(e) and 2(g) and SM [13]. This crucial rule was overlooked in [12]. (iv) Vertex interactions: they are determined by the channel geometry and must be measured experimentally. As the fluid exits a node and enters a channel where $J \neq 0$, the deformations of the active flow that formed at the vertex relax to yield a laminar flow. These deformations do not propagate to the adjacent node; see Fig. 1(e). As a result two vertices connected by an edge where $J \neq 0$ are essentially decoupled. This reasoning explains why the rules (i), (ii), and (iii) are enough to account for all our measurements in square-grid and hexagonal networks [13]. However, along edges where $J = 0$ vortices form. The continuity of the flow field at the subchannel level hence couples the handedness of the vortices to the flow configurations in the adjacent nodes. This coupling defines the vertex interaction rules discussed in [12].

From a practical perspective, the four active-hydraulic rules provide a cost effective solution to generate active-flow configurations. The strategy is simple. It consists of generating spin configurations on a lattice by minimizing a cost function that enforces rules (i)–(iv). Sampling active-flow configurations reduces to sampling the ground states of vertex models. From a more fundamental perspective, active hydraulics is in a one-to-one correspondence with the statistical mechanics of interacting loop models that is a topic of intense studies both in theoretical physics and mathematics. To date, however, most predictions focus on 2D loop ensembles and therefore to 2D active hydraulic. Predicting the geometry of the active flows in tridimensional pipe networks hence remains both a formidable theoretical and experimental challenge.

Acknowledgments—We thank Amélie Chardac and Alexis Poncet for fruitful interactions. This work was partly supported by the European Research Council (ERC) under the European Union's Horizon 2020 Research and Innovation Program (Grant Agreement no. [101019141]) (D. B. and C. J.).

[1] E. H. Lieb, Phys. Rev. **162**, 162 (1967).
[2] R. J. Baxter, *Exactly Solved Models in Statistical Mechanics* (Elsevier, New York, 2016).
[3] L. Pauling, J. Am. Chem. Soc. **57**, 2680 (1935).
[4] J.-B. Zuber, in *Fields, Strings and Critical Phenomena (Les Houches 1988)* (Elsevier, New York, 1988), pp. 249–279.
[5] J. L. Jacobsen, in *Polygons, Polyominoes and Polycubes* (Springer, New York, 2009), pp. 347–424, 10.1007/978-1-4020-9927-4_14.
[6] P. Zinn-Justin, arXiv:0901.0665.
[7] J. L. Jacobsen and J. Kondev, Nucl. Phys. **B532**, 635 (1998).
[8] B. Duplantier, Phys. Rev. Lett. **84**, 1363 (2000).
[9] G. Kuperberg, Int. Math. Res. Not. **1996**, 139 (1996).
[10] R. J. Baxter, S. B. Kelland, and F. Y. Wu, J. Phys. A **9**, 397 (1976).
[11] A. Bricard, J.-B. Caussin, N. Desreumaux, O. Dauchot, and D. Bartolo, Nature (London) **503**, 95 (2013).
[12] C. Jorge, A. Chardac, A. Poncet, and D. Bartolo, Nat. Phys. **20**, 303 (2024).
[13] See Supplemental Material at http://link.aps.org/supplemental/10.1103/PhysRevLett.134.188302 for a description of the experiment, an introduction to the mappings between vertex and loop models, and additional experimental results on triangular and snub square networks, which includes Refs. [2,14–23].
[14] P. J. Lu, P. A. Sims, H. Oki, J. B. Macarthur, and D. A. Weitz, Opt. Express **15**, 8702 (2007).
[15] D. Blair and E. Dufresne, Particle-tracking code available at http://physics.georgetown.edu/matlab (2008).
[16] E. Stamhuis and W. Thielicke, J. Open Res. Software **2**, 30 (2014).
[17] A. Lafay, Geometrical lattice models, algebraic spiders and applications to random geometry, Ph.D. thesis, Sorbonne Université, 2022.
[18] B. Nienhuis, Phase Transitions Crit. Phenom. **11**, 1 (1987).
[19] M. Henkel and D. Karevski, *Conformal Invariance: An Introduction to Loops, Interfaces and Stochastic Loewner Evolution* (Springer Science & Business Media, Berlin Heidelberg, 2012), Vol. 853.
[20] T. Grossman and A. Aharony, J. Phys. A **19**, L745 (1986).
[21] R. J. Baxter, J. Math. Phys. (N.Y.) **10**, 1211 (1969).
[22] S. B. Kelland, Aust. J. Phys. **27**, 813 (1974).
[23] B. Nienhuis, Phys. Rev. Lett. **49**, 1062 (1982).
[24] A. Morin and D. Bartolo, Phys. Rev. X **8**, 021037 (2018).
[25] F. G. Woodhouse, A. Forrow, J. B. Fawcett, and J. Dunkel, Proc. Natl. Acad. Sci. U.S.A. **113**, 8200 (2016).
[26] H. Wioland, E. Lushi, and R. E. Goldstein, New J. Phys. **18**, 075002 (2016).

[27] K.-T. Wu, J. B. Hishamunda, D. T. Chen, S. J. DeCamp, Y.-W. Chang, A. Fernández-Nieves, S. Fraden, and Z. Dogic, Science **355**, eaal1979 (2017).
[28] J. Hardoüin, J. Laurent, T. Lopez-Leon, J. Ignés-Mullol, and F. Sagués, Soft Matter **16**, 9230 (2020).
[29] M. Udagawa and L. Jaubert, *Spin Ice*, (Springer International Publishing, New York, 2021), 10.1007/978-3-030-70860-3.
[30] F. G. Woodhouse and J. Dunkel, Nat. Commun. **8**, 15169 (2017).
[31] F. G. Woodhouse, J. B. Fawcett, and J. Dunkel, New J. Phys. **20**, 035003 (2018).
[32] Y.-N. Young and M. J. Shelley, Phys. Rev. Lett. **99**, 058303 (2007).
[33] E. Wandersman, N. Quennouz, M. Fermigier, A. Lindner, and O. Du Roure, Soft Matter **6**, 5715 (2010).
[34] H. Saleur and B. Duplantier, Phys. Rev. Lett. **58**, 2325 (1987).
[35] M. Kolb and M. Rosso, Phys. Rev. E **47**, 3081 (1993).
[36] M. Aizenman, B. Duplantier, and A. Aharony, Phys. Rev. Lett. **83**, 1359 (1999).
[37] J. Kondev, J. de Gier, and B. Nienhuis, J. Phys. A **29**, 6489 (1996).
[38] Y. M. M. Knops, B. Nienhuis, H. J. F. Knops, and H. W. J. Blöte, Phys. Rev. B **50**, 1061 (1994).